

Ferrofluid annulus in crossed magnetic fieldsPedro O. S. Livera ^{1,*}, Pedro H. A. Anjos ^{2,†} and José A. Miranda ^{1,‡}¹*Departamento de Física, Universidade Federal de Pernambuco, Recife, Pernambuco 50670-901 Brazil*²*Department of Applied Mathematics, Illinois Institute of Technology, Chicago, Illinois 60616, USA*

(Received 6 January 2022; accepted 6 April 2022; published 21 April 2022)

We study the dynamics and pattern formation of a ferrofluid annulus enveloped by two nonmagnetic fluids in a Hele-Shaw cell, subjected to an in-plane crossed magnetic field configuration involving the combination of radial and azimuthal magnetic fields. A perturbative, second-order mode-coupling analysis is employed to investigate how the ferrofluid annulus responds to variations in the relative strength of the radial and azimuthal magnetic field components, as well as in the thickness of magnetic fluid ring. By tuning the magnetic field components and the annulus' thickness, we have found the development of several stationary annular shapes, presenting polygon-shaped structures typically having skewed, peaked fingers. Such fingered structures may vary their skewness, sharpness, and number and arise on the inner, outer, or even both boundaries of the annulus. In addition to controlling the morphologies of the ferrofluid annuli, the external field can be used to put the annulus into a rotational motion, with an angular velocity having prescribed magnitude, and direction. Our second-order theory is utilized to obtain a correction to the linear stability analysis prediction of such angular velocity, usually resulting in a decreased weakly nonlinear value as compared with the magnitude predicted by purely linear theory. These theoretical results suggest the use of magnetic-field-controlled ferrofluid annuli in Hele-Shaw cells as a potential laboratory for microscale applications related to the manipulation of shape-programmable magnetic fluid objects and tunable fluidic-mixing devices in confined environments.

DOI: [10.1103/PhysRevE.105.045106](https://doi.org/10.1103/PhysRevE.105.045106)**I. INTRODUCTION**

Ferrofluids are functional and smart fluid materials capable of changing their shape in the presence of an external magnetic field. These smart fluids are stable colloidal suspensions where nanometer-sized magnetic monodomain particles are dispersed in a nonmagnetic carrier fluid [1–3]. While ferrofluids behave like regular Newtonian fluids in the absence of an external magnetic field, once a magnetic field is applied, the tiny magnetic particles within the fluid respond superparamagnetically, aligning with the applied field. This allows an easy and versatile manipulation of the ferrofluid's flow and shape via magnetic means. Because of their unique material features, ferrofluids have been widely studied from the most fundamental aspects to a wide range of applications. In fact, ferrofluids have attracted increasing interest in various scientific research areas including physics, chemistry, engineering, material science, biology, and medicine [4–9].

During the past few years, ferrofluids have gained significant attention because of their relevance to cutting edge technologies in biomedicine such as in localized heating (hyperthermia), cancer treatment, and target drug delivery [10,11], mechanics of tissues [12–14], microfluidics and micromixing [15,16], and in the dynamics and control of soft robots [17,18]. All these important applications take

advantage of the distinctive ferrofluid material properties to achieve multiple functionalities. For instance, one can use various magnetic field configurations to actuate and control ferrofluid droplets as shape-programmable magnetic fluid objects, which can move through narrow channels, transporting liquid samples and mixing chemicals in confined environments. This enables on demand liquid-cargo delivery, morphing for effective and adjustable handling of fragile objects and manipulable fluidic-mixing function. One very interesting capability of such ferrofluid controllable tools has been described in Refs. [19,20] where ferrofluid droplets could be programmed into a ring shape which could trap, transport, and release multiple delicate objects efficiently.

Due to their singular liquid and magnetic properties, ferrofluids can navigate through constrained, effectively two-dimensional passages, exhibiting several magnetically controlled, complex shape-morphing behaviors. These appealing pattern-forming phenomena arise due to the interplay among pressure, surface tension, and magnetic forces [1–3]. These features make ferrofluids a remarkable material to study a variety of interfacial instabilities and pattern formation processes in spatially confined environments. Therefore, ferrofluids are a natural choice for investigating the dynamics of pattern-forming structures in the confined geometry of Hele-Shaw cells [21–23]. The Hele-Shaw cell apparatus [24,25] consists of two parallel glass plates separated by a narrow gap, where the ferrofluid can flow under the action of an applied magnetic field. Over the years, investigators have analyzed a vast number of ferrofluid interfacial instabil-

*pedro.livera@ufpe.br

†pamorimanjos@iit.edu

‡jose.mirandant@ufpe.br

ity problems in Hele-Shaw cells, under the action of several different magnetic field configurations.

One iconic example of such pattern-forming phenomena in confined ferrofluids is the development of the so-called labyrinthine instability [26–29], where highly branched patterns are formed when a ferrofluid droplet, surrounded by a nonmagnetic fluid, is trapped in the Hele-Shaw cell under a uniform magnetic field applied perpendicularly to the cell's plates. This perpendicular magnetic field configuration is generated by a pair of identical Helmholtz coils whose currents are equal and flow in the same directions. The perpendicular field aligns the tiny magnetic moments of the ferrofluid in a direction normal to the plates. These magnetic moments repel each other, and the interface deforms. On the other hand, surface tension forces tend to stabilize the two-fluid interface. The complex interrelation of these magnetic and surface tension effects ultimately leads to the emergence of intricate maze-like, labyrinthine patterns.

Two other particularly interesting magnetic field arrangements in Hele-Shaw cells with ferrofluids are the ones related to the influence of azimuthal and radial applied magnetic fields. The azimuthal magnetic field configuration is produced by a current-carrying wire which is normal to the cell plates and passes through its center [30]. This generates a magnetic field in the plane of the cell that turns around the wire, producing a magnetic body force directed radially inward [1,31]. This force tends to attract a ferrofluid sample toward the current-carrying wire. For a Hele-Shaw cell containing a ferrofluid and a nonmagnetic fluid, the azimuthal magnetic field can act to either stabilize or destabilize the fluid-fluid interface. If the ferrofluid is the inner fluid, then the azimuthal field tends to stabilize the two-fluid interface. This azimuthal field stabilizing strategy has been proven effective to hinder interfacial instabilities in ferrofluids under centrifugally driven fingering in rotating Hele-Shaw cells [30]. On the other hand, if the ferrofluid is the outer fluid, then the interface will tend to distort, resulting in different types of patterns ranging from regular, steady-state fingering shapes presenting flat tips [32] through considerably convoluted time-varying fingered structures [33].

The action of an in-plane, externally applied radial magnetic field on confined ferrofluid droplets has also been studied. Similarly to the case of the labyrinthine instability [26–29], the radial magnetic field is also produced by two Helmholtz coils but now carrying electric currents that flow in opposite directions [34]. Under these conditions, the magnetic body force tends to destabilize the interface separating the magnetic and nonmagnetic fluids, while surface tension acts to stabilize it. The competition of these physical effects result in the appearance of various types of polygon-shaped as well as starfishlike patterns [35,36]. Furthermore, researchers have also analyzed the simultaneous influence of both azimuthal and radial applied fields on the behavior of ferrofluid droplets. Recently, fully nonlinear simulations have been utilized to investigate the behavior of ferrofluid droplets in a Hele-Shaw cell subjected to such a crossed magnetic field arrangement [37,38]. These studies revealed that, by tuning the strength of the azimuthal and radial fields, one observes the development of appealing skewed shaped, rotating ferrofluid patterns having both stable (immutable) and unstable (ever changing) profiles.

Irrespective of the scientific relevance and significant number of investigations on the topic of interfacial ferrofluid patterns in Hele-Shaw cells (Refs. [26–38] and references therein), the almost absolute majority of existing studies focuses on the situation in which the region occupied by the ferrofluid is simply connected. Nevertheless, as discussed in Refs. [19,20] ring-shaped ferrofluid droplets are useful controlling tools in the sense that they can be used to trap, transport, and release multiple delicate objects efficiently in confined spaces. On the practical side [19,20], the magnetic manipulation of such ferrofluid annular structures potentially enables unprecedented functionalities in laboratory and organ-on-a-chip, fluidics, bioengineering, and medical device applications. On the academic side, the ferrofluid annulus setup is of special interest because it involves the interplay between two disjoint interfaces (the inner and outer boundaries of the ferrofluid ring), something that potentially can lead to new phenomenology and still unexplored dynamical behaviors not available in the conventional situation in which a magnetic and a nonmagnetic fluid are separated by a single interface. Despite the importance of the study of the dynamics and pattern formation of doubly connected, annular ferrofluid domains in Hele-Shaw cells, this topic has been largely unexplored in the literature. As a matter of fact, only very recently investigators started to examine this particular situation [39]. More precisely, Ref. [39] analyzed the flow of a viscous ferrofluid annulus surrounded by two nonmagnetic fluids in a Hele-Shaw cell, subjected to an external radial magnetic field. It has been shown that the nonlinear coupling between inner and outer disjoint boundaries of the ferrofluid annulus results in the formation of motionless, stationary-state polygonal-like annular shapes, presenting sharp fingers.

Building on our previous work on a ferrofluid annulus under a radial field [39] and motivated by the stimulating results obtained in Refs. [37,38] for the simply connected case of a ferrofluid droplet under a crossed magnetic field, in this work we consider an even more complex situation: a ferrofluid annulus enveloped by nonmagnetic fluids, confined in a Hele-Shaw cell, and subjected by the concurrent effect of both radial and azimuthal magnetic fields. The use of such crossed magnetic fields configuration adds considerable versatility into the system, allowing separate bidirectional magnetic tuning of the inner and outer interfaces of the ferrofluid annular ring. By tuning the azimuthal and radial fields one can trigger distinct instability behaviors at the disjoint interfaces of the ferrofluid annulus. This enriches the physical problem at hand. For example, depending on the relative strength of the azimuthal and radial fields, one can make the inner or the outer interface more or less unstable. As a consequence, one can magnetically induce changes in the instability and shape of the interfaces, without having to alter the fluids positions or material properties (e.g., viscosities, densities, etc.). In addition, the crossed magnetic fields can be used to control the magnitude and direction of the ferrofluid annulus rotational speed. All these magnetic controlling capabilities could be eventually useful to a number of possible applications [10–20].

We tackle the problem by employing a perturbative, nonlinear (second-order) mode-coupling analysis. In this framing, and by adjusting the fields' relative magnitudes, we examine how the spinning ferrofluid annulus responds to variations

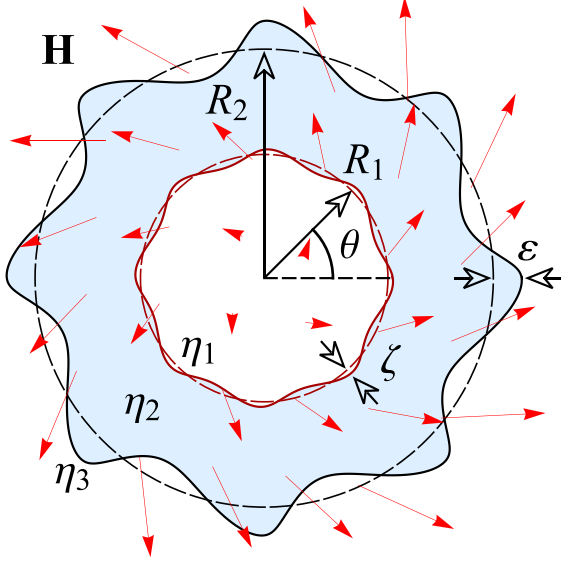


FIG. 1. Schematic of the ferrofluid annulus confined flow problem under the action of crossed magnetic fields (radial and azimuthal). Initially, the ferrofluid annular structure has circular boundaries of radii R_1 and R_2 (dashed circles). The ferrofluid annulus has viscosity η_2 , while the inner and outer fluids are nonmagnetic, having viscosities η_1 , and η_3 , respectively. The combined magnetic field \mathbf{H} may deform the inner and outer interfaces of the ferrofluid annulus (solid curves). The interfacial perturbation amplitudes in the distorted ferrofluid ring structure are denoted by $\zeta = \zeta(\theta, t)$ and $\varepsilon = \varepsilon(\theta, t)$, where θ is the azimuthal angle.

on its thickness. Additionally, for a given thickness, we investigate how the magnetic fluid annulus morphology, and its rotational dynamics are affected by the crossed magnetic fields at the onset of nonlinearities.

II. PHYSICAL PROBLEM AND GOVERNING EQUATIONS

In this section, we develop a perturbative mode-coupling theory to describe the magnetically induced instabilities emerging on the boundaries of an initially circular ferrofluid ring of viscosity η_2 , delimited by unperturbed radii R_1 (inner) and R_2 (outer), and surrounded by two nonmagnetic fluids of viscosities η_1 and η_3 (see Fig. 1). All the fluids are immiscible, incompressible, and Newtonian and bound to flow between the plates of a Hele-Shaw cell of gap thickness b . In this ferrohydrodynamic problem, the inner and outer interfaces of the ferrofluid annulus have surface tensions σ_{12} and σ_{23} , respectively, and the dual-interface system is subjected to a two-component, externally applied magnetic field [37,38],

$$\mathbf{H} = H_0 r \hat{\mathbf{r}} + \frac{I}{2\pi r} \hat{\boldsymbol{\theta}}. \quad (1)$$

In Eq. (1), the first (second) term on the right-hand side represents the applied radial (azimuthal) magnetic field and $\hat{\mathbf{r}}$ ($\hat{\boldsymbol{\theta}}$) is a unit vector in the radial (azimuthal) direction. In addition, H_0 is a constant, r is the radial distance from the origin of the coordinate system (located at the center of the cell), and the Hele-Shaw cell is located at the mid-distance between a pair of identical Helmholtz coils, whose electric currents are equal and flow in opposite directions. These coils

are responsible for generating the radial magnetic field, while a wire perpendicular to the coils, and carrying an electric current I , passes through the center of the Hele-Shaw cell, producing the azimuthal magnetic field.

After neglecting inertial effects and averaging across the Hele-Shaw cell's gap, the fluids' velocities are governed by the modified Darcy's law [26–28],

$$\mathbf{v}_j = -\frac{b^2}{12\eta_j} \nabla(p_j - \Psi_j), \quad (2)$$

and the incompressibility condition,

$$\nabla \cdot \mathbf{v}_j = 0, \quad (3)$$

where $p_j = p_j(r, \theta)$ and Ψ_j are the gap-averaged pressure and scalar potential, respectively. This scalar potential accounts for the magnetic body forces arising in the system as a response of the ferrofluid annulus to the applied magnetic field \mathbf{H} , and it is written as

$$\Psi_j = \frac{\mu_0 \chi H^2}{2}, \quad (4)$$

with μ_0 denoting the magnetic permeability of free space and $H = |\mathbf{H}|$ representing the combined magnetic field intensity. In addition, χ is the ferrofluid's constant magnetic susceptibility, which is nonzero only for the intermediate annulus. Therefore, $\Psi_1 = \Psi_3 = 0$ for the nonmagnetic inner and outer fluids. The subscripts $j = 1, 2$, and 3 refer to the inner, intermediate (annulus), and outer fluids, respectively.

The pressure field is discontinuous across the two interfaces of the system due to the presence of the surface tensions and the unequal normal component of the ferrofluid's magnetization \mathbf{M} on either side of the annulus. These two pressure jumps, one for each interface, are given by modified Young-Laplace equations [1,2],

$$(p_1 - p_2)|_{r=R_1} = [\sigma_{12}\kappa_{12} + \frac{1}{2}\mu_0(\mathbf{M} \cdot \hat{\mathbf{n}})^2]|_{r=R_1}, \quad (5)$$

and

$$(p_2 - p_3)|_{r=R_2} = [\sigma_{23}\kappa_{23} - \frac{1}{2}\mu_0(\mathbf{M} \cdot \hat{\mathbf{n}})^2]|_{r=R_2}, \quad (6)$$

where κ_{12} and κ_{23} denote the interfacial curvatures [39] of the inner and outer interfaces in the plane of the Hele-Shaw cell, respectively. In addition, $\hat{\mathbf{n}}|_{r=R_{1,2}}$ represents the unit normal vectors at the interfaces, with $\mathcal{R}_1 = \mathcal{R}_1(\theta, t)$ [$\mathcal{R}_2 = \mathcal{R}_2(\theta, t)$] being the position of the perturbed inner (outer) interface. We demonstrate how to obtain the functions \mathcal{R}_1 and \mathcal{R}_2 in a perturbative fashion later in this section. The term proportional to $(\mathbf{M} \cdot \hat{\mathbf{n}})^2$ on the right-hand side of Eqs. (5) and (6) is commonly known as the magnetic normal traction term [1,2] and incorporates the influence of the discontinuous normal component of the magnetization at the interfaces. Consistently with previous studies, here we assume that the ferrofluid is uniformly magnetized and that the magnetization is collinear with the external magnetic field, i.e., $\mathbf{M} = \chi \mathbf{H}$ [1,2,26–28].

Unlike the pressure field discontinuities expressed by Eqs. (5) and (6), kinematic boundary conditions [25] state the continuity of the normal flow velocity as one crosses each one of the interfaces. These relations supplement the boundary

conditions (5) and (6) and are expressed as

$$\frac{\partial \mathcal{R}_1}{\partial t} = \left(\frac{1}{r^2} \frac{\partial \mathcal{R}_1}{\partial \theta} \frac{\partial \phi_j}{\partial \theta} \right) \Big|_{r=\mathcal{R}_1} - \left(\frac{\partial \phi_j}{\partial r} \right) \Big|_{r=\mathcal{R}_1} \quad (7)$$

for the inner interface (with $j = 1, 2$) and

$$\frac{\partial \mathcal{R}_2}{\partial t} = \left(\frac{1}{r^2} \frac{\partial \mathcal{R}_2}{\partial \theta} \frac{\partial \phi_j}{\partial \theta} \right) \Big|_{r=\mathcal{R}_2} - \left(\frac{\partial \phi_j}{\partial r} \right) \Big|_{r=\mathcal{R}_2} \quad (8)$$

for the outer interface (with $j = 2, 3$). Note that governing Eq. (2) implies that the flow is irrotational ($\nabla \times \mathbf{v}_j = 0$), allowing one to state the problem in terms of velocity potentials $\phi_j(r, \theta)$ ($\mathbf{v}_j = -\nabla \phi_j$), which appear in the kinematic boundary conditions (7) and (8). Moreover, the extra governing Eq. (3) implies that these potentials obey Laplace's equations $\nabla^2 \phi_j = 0$ [39].

After presenting the governing equations of the problem [Eqs. (2) and (3)] and the boundary conditions at the interfaces [Eqs. (5)–(8)], we have all the necessary elements to perform our nonlinear mode-coupling analysis of the problem. Therefore, we first represent the perturbed, time-dependent position of the inner interface as $\mathcal{R}_1 = R_1 + \zeta(\theta, t)$, where θ denotes the azimuthal angle in the r - θ plane (Fig. 1). The net interface disturbance is expressed by a Fourier series

$$\zeta(\theta, t) = \sum_{n=-\infty}^{+\infty} \zeta_n(t) e^{in\theta}, \quad (9)$$

where $\zeta_n(t)$ denotes the complex Fourier amplitudes, with integer wave numbers n . Likewise, the perturbed outer interface shape is given by $\mathcal{R}_2 = R_2 + \varepsilon(\theta, t)$, where

$$\varepsilon(\theta, t) = \sum_{n=-\infty}^{+\infty} \varepsilon_n(t) e^{in\theta}. \quad (10)$$

Since we are mainly interested in exploring the early nonlinear behavior of the annular system beyond the linear stage of the dynamics, our perturbative approach keeps terms up to second order in ζ and ε . In both the Fourier expansions of ζ and ε , we include the $n = 0$ mode to maintain the area of the intermediate ferrofluid layer independent of the perturbations. Mass conservation imposes that the zeroth mode is written in terms of the other modes as $\zeta_0 = -(1/2R_1) \sum_{n=1}^{\infty} [|\zeta_n(t)|^2 + |\zeta_{-n}(t)|^2]$ [39]. Similarly, we have $\varepsilon_0 = -(1/2R_2) \sum_{n=1}^{\infty} [|\varepsilon_n(t)|^2 + |\varepsilon_{-n}(t)|^2]$.

Due to the presence of the crossed magnetic field configuration, the interfaces may deform, and their time-dependent shapes, as well as the ferrofluid annulus behavior, are determined by the interplay of stabilizing and destabilizing forces acting on the system. Therefore, to gain access to these nonlinear aspects of the flow, it is evident that one needs to find how the Fourier amplitudes $\zeta_n(t)$ and $\varepsilon_n(t)$ evolve in time. The differential equations governing the time evolution of these perturbation amplitudes are found as follows: We first consider $|\zeta| \ll R_1$ and $|\varepsilon| \ll R_2$, and then we perform Fourier expansions for the velocity potentials, using the kinematic boundary conditions [Eqs. (7) and (8)] to express the Fourier coefficients of ϕ_j in terms of ζ_n , ε_n , and their time derivatives. Substituting these relations, and the pressure jump conditions [Eqs. (5) and (6)] into Darcy's law [Eq. (2)], and keeping terms up to second order in ζ and ε , we obtain the set of

dimensionless coupled equations of motion for both the perturbation amplitudes ζ_n and ε_n (for $n \neq 0$),

$$\begin{aligned} \dot{\zeta}_n &= f_1 \Lambda(n) \zeta_n + f_2 \Gamma(n) \varepsilon_n \\ &+ f_1 \sum_{n' \neq 0} [F(n, n') \zeta_{n'} \zeta_{n-n'} + G(n, n') \dot{\zeta}_{n'} \zeta_{n-n'}] \\ &+ f_2 \sum_{n' \neq 0} [H(n, n') \varepsilon_{n'} \varepsilon_{n-n'} + I(n, n') \dot{\varepsilon}_{n'} \varepsilon_{n-n'}] \\ &+ f_2 \sum_{n' \neq 0} [J(n, n') \dot{\zeta}_{n'} \varepsilon_{n-n'} + K(n, n') \dot{\varepsilon}_{n'} \zeta_{n-n'}], \quad (11) \end{aligned}$$

and

$$\begin{aligned} \dot{\varepsilon}_n &= f_3 \Lambda(n) \zeta_n + f_4 \Gamma(n) \varepsilon_n \\ &+ f_4 \sum_{n' \neq 0} [\mathcal{F}(n, n') \varepsilon_{n'} \varepsilon_{n-n'} + \mathcal{G}(n, n') \dot{\varepsilon}_{n'} \varepsilon_{n-n'}] \\ &+ f_3 \sum_{n' \neq 0} [\mathcal{H}(n, n') \zeta_{n'} \zeta_{n-n'} + \mathcal{I}(n, n') \dot{\zeta}_{n'} \zeta_{n-n'}] \\ &+ f_3 \sum_{n' \neq 0} [\mathcal{J}(n, n') \dot{\varepsilon}_{n'} \zeta_{n-n'} + \mathcal{K}(n, n') \dot{\zeta}_{n'} \varepsilon_{n-n'}], \quad (12) \end{aligned}$$

where the overdot represents a total time derivative. In Eqs. (11) and (12) lengths and time are rescaled by $L = r_0$ and $T = 12(\eta_3 + \eta_2)r_0^3/\sigma_{23}b^2$, respectively, where r_0 is a characteristic length being on the order of the unperturbed radii R_1 and R_2 . From this point on, unless otherwise stated, we use a dimensionless version of the equations.

Although the time-independent, complex functions

$$\begin{aligned} \Lambda(n) &= \mathcal{A}|n| \left[-\frac{\sigma}{R_1^3} (n^2 - 1) - \chi(1 + \chi) N_{\text{Br}} \right. \\ &\left. + \chi \frac{N_{\text{Ba}}}{R_1^4} + in\chi^2 \text{sgn}(I) \frac{\sqrt{N_{\text{Br}} N_{\text{Ba}}}}{R_1^2} \right], \quad (13) \end{aligned}$$

and

$$\begin{aligned} \Gamma(n) &= |n| \left[-\frac{1}{R_2^3} (n^2 - 1) + \chi(1 + \chi) N_{\text{Br}} \right. \\ &\left. - \chi \frac{N_{\text{Ba}}}{R_2^4} - in\chi^2 \text{sgn}(I) \frac{\sqrt{N_{\text{Br}} N_{\text{Ba}}}}{R_2^2} \right] \quad (14) \end{aligned}$$

emerge at the linear level (i.e., first order in ζ_n and ε_n), we stress that these functions are not the linear growth rates of the system, which will be derived later in this section. The relative strengths of radial and azimuthal magnetic forces to the capillary force are represented by the magnetic Bond numbers

$$N_{\text{Br}} = \frac{\mu_0 H_0^2 r_0^3}{\sigma_{23}}, \quad \text{and} \quad N_{\text{Ba}} = \frac{\mu_0}{\sigma_{23} r_0} \left(\frac{I}{2\pi} \right)^2,$$

respectively. In addition,

$$f_1 = \frac{1 - A_{23} R^{2|n|}}{1 + A_{12} A_{23} R^{2|n|}}, \quad f_2 = \frac{1 + A_{12}}{1 + A_{12} A_{23} R^{2|n|}} R^{|n|-1},$$

$$f_3 = \frac{1 - A_{23}}{1 + A_{12} A_{23} R^{2|n|}} R^{|n|+1}, \quad f_4 = \frac{1 + A_{12} R^{2|n|}}{1 + A_{12} A_{23} R^{2|n|}},$$

where $A_{12} = (\eta_2 - \eta_1)/(\eta_2 + \eta_1)$ [$A_{23} = (\eta_3 - \eta_2)/(\eta_3 + \eta_2)$] is the viscosity contrast of fluids 1 and 2 [2 and 3],

$\mathcal{A} = (\eta_3 + \eta_2)/(\eta_2 + \eta_1)$, and $\sigma = \sigma_{12}/\sigma_{23}$. The parameter R appearing in f_1, f_2, f_3 , and f_4 is defined as

$$R = \frac{R_1}{R_2}, \quad (15)$$

and it quantifies the coupling strength between the interfaces of the system [39]. Therefore, it is evident that the terms proportional to f_2 and f_3 on the right-hand side of the two ordinary differential equations (ODEs) (11) and (12) couple the interfacial motivations, meaning that any disturbance growing in one of the interfaces may impact the dynamics of the other, already at the linear level. The nonlinear mode-coupling functions $F, G, H, I, J, K, \mathcal{F}, \mathcal{G}, \mathcal{H}, \mathcal{I}, \mathcal{J}$, and \mathcal{K} appearing on the right-hand side of Eqs. (11) and (12) are given in the Appendix [see Eqs. (A1)–(A16)].

It should be clear that while dealing with Eqs. (11) and (12) [and with the associated functions given in Eqs. (A1)–(A16)], we have reduced the fully nonlinear problem to an abbreviated perturbative version in which terms beyond quadratic ones have been dropped. Within our perturbative approach, the contributions coming from higher perturbative orders (e.g., third, fourth, etc.) are less prevalent than the first- and second-order ones, due to the smallness of ζ_n and ε_n with respect to the unperturbed radii R_1 and R_2 of the ferrofluid annulus. Nevertheless, these neglected higher-order contributions can still provide noticeable improvements in the morphological and dynamical agreement between weakly nonlinear perturbative solutions and fully nonlinear results. As expected, the consideration of perturbative terms beyond second order for this doubly connected system is not trivial to implement, and would make the mode-coupling equations very lengthy and considerably cluttered. As will become evident during the course of this work, despite the intrinsic limitations of this truncated perturbative approach, our second-order mode-coupling scheme is still able to capture valuable nonlinear information about the system. Alternative asymptotic processes [40] could have been employed to obtain a system of weakly nonlinear equations for the problem. For instance, we could have assumed that the system is near the instability threshold, and derived equations for the amplitudes through a central manifold reduction [41,42]. This method would indeed be more systematic. However, we believe that it would not lead to any new behavior, as Eqs. (11) and (12) already include all second-order terms of the problem, though some of them might happen to be spurious. Moreover, as we will see in Sec. III, all the solutions reach steady states, and the amplitudes remain very small. This further indicates that higher-order terms can be dropped in the asymptotic regime of interest. Therefore, we believe that the rationale behind Eqs. (11) and (12) is sufficiently clear and more technical analyses of the problem are beyond the scope of this work.

Note that due to the somewhat complicated format of expressions (11) and (12), especially because of their coupled nature, it is difficult to extract analytical information about the physical effects of the different dimensionless parameters on each interface, and make predictions about the system's general behavior. Nevertheless, a considerably simpler but yet useful scenario is obtained when one considers the limiting case of decoupled interfaces, also known as the two-fluid single-interface limit [39,43,44]. In such a limit, the interfacial

motions are independent of each other, allowing one to study, for instance, the physical impact of the main dimensionless parameters (N_{Br} and N_{Ba}) on the stability of the decoupled interfaces. Furthermore, the information provided by the decoupled limit helps one to understand some of the behaviors occurring in the annular coupled system, which is our main goal in the current work. As a matter of fact, analyzing the Eqs. (11) and (12) in this limit case is also a good exercise to check the consistency and correctness of our main analytical results, as it permits the direct comparison with other works already published in the literature. Therefore, in the limit of a thick annulus [i.e., $R \rightarrow 0$ such that $(f_1, f_4) \rightarrow 1$, and $(f_2, f_3) \rightarrow 0$] the ODEs (11) and (12) decouple, leaving two separate single interfaces whose perturbations are described by

$$\begin{aligned} \dot{\zeta}_n &= \Lambda(n) \zeta_n \\ &+ \sum_{n' \neq 0} [F(n, n') \zeta_{n'} \zeta_{n-n'} + G(n, n') \dot{\zeta}_{n'} \zeta_{n-n'}] \end{aligned} \quad (16)$$

and

$$\begin{aligned} \dot{\varepsilon}_n &= \Gamma(n) \varepsilon_n \\ &+ \sum_{n' \neq 0} [\mathcal{F}(n, n') \varepsilon_{n'} \varepsilon_{n-n'} + \mathcal{G}(n, n') \dot{\varepsilon}_{n'} \varepsilon_{n-n'}]. \end{aligned} \quad (17)$$

Equation (16) describes the interfacial behavior of a non-magnetic fluid droplet with viscosity η_1 surrounded by a ferrofluid with viscosity η_2 , where $\Lambda(n)$ [Eq. (13)] is the time-independent growth rate of the flow. Likewise, Eq. (17) represents the interface behavior of a ferrofluid droplet with viscosity η_2 surrounded by a nonmagnetic fluid with viscosity η_3 , where $\Gamma(n)$ [Eq. (14)] is the time-independent growth rate. By analyzing $\Lambda(n)$, we observe that both the surface tension and the radial magnetic field component act to restrain interfacial instability, while the azimuthal magnetic field component promotes its growth. The presence of an imaginary part in Eq. (13) is responsible for the propagation of the perturbed interfacial shape, with linear phase velocity given by $V_1(n) = -\text{Im}[\Lambda(n)]/n = -\chi^2 \text{sgn}(I) \mathcal{A} |n| \sqrt{N_{Br} N_{Ba}} / R_1^2$. This wave propagation is manifested as a clockwise rotation of the confined droplet and only occurs in the presence of the crossed magnetic field configuration, i.e., for $N_{Br} \neq 0$ and $N_{Ba} \neq 0$. On the other hand, in $\Gamma(n)$, surface tension still acts as a stabilizing effect, but the magnetic field components play interchanged roles: While the radial magnetic field destabilizes the interface, the azimuthal magnetic field tries to keep a circular interfacial shape. In addition, the wave propagation with linear phase velocity $V_2(n) = -\text{Im}[\Gamma(n)]/n = \chi^2 \text{sgn}(I) |n| \sqrt{N_{Br} N_{Ba}} / R_2^2$ promotes a counterclockwise rotation of the droplet. These interfacial behaviors, as well as the physical impact of the system's dimensionless parameters on the stability of interfaces, are in agreement with previous works related to two-fluid, single-interface, magnetic field-induced flow problems in Hele-Shaw cells [37,38].

As the last result of this section, we derive the linear growth rates associated with each interface on the boundaries of the ferrofluid annulus. At the linear level of the dynamics, the perturbation amplitudes ζ_n and ε_n are so small that second-order terms in Eqs. (11) and (12) can be neglected, yielding

$$\dot{\zeta}_n = f_1 \Lambda(n) \zeta_n + f_2 \Gamma(n) \varepsilon_n, \quad (18)$$

and

$$\dot{\varepsilon}_n = f_3 \Lambda(n) \zeta_n + f_4 \Gamma(n) \varepsilon_n. \quad (19)$$

This system of coupled first-order ODEs with constant (in time) coefficients can be easily solved by first isolating ε_n in Eq. (18), and then substituting the new expression in Eq. (19). The resulting equation is a second-order ODE for ζ_n , whose solution

$$\zeta_n(t) = \frac{\zeta_n(0)}{2\delta(n)} \{ [f_1 \Lambda(n) + (2f_2 - f_4) \Gamma(n)] f_-(n, t) + \delta(n) f_+(n, t) \} \quad (20)$$

is readily obtained. Finally, by substituting the previous result back into Eq. (18), we have

$$\varepsilon_n(t) = \frac{\varepsilon_n(0)}{2\delta(n)} \{ [(2f_3 - f_1) \Lambda(n) + f_4 \Gamma(n)] f_-(n, t) + \delta(n) f_+(n, t) \}, \quad (21)$$

where

$$\delta(n) = \sqrt{[f_1 \Lambda(n) - f_4 \Gamma(n)]^2 + 4f_2 f_3 \Lambda(n) \Gamma(n)}, \quad (22)$$

and

$$f_{\pm}(n, t) = \exp \left\{ \frac{t}{2} [f_1 \Lambda(n) + f_4 \Gamma(n) + \delta(n)] \right\} \pm \exp \left\{ \frac{t}{2} [f_1 \Lambda(n) + f_4 \Gamma(n) - \delta(n)] \right\}. \quad (23)$$

We point out that the approach employed above to solve the system composed of Eqs. (18) and (19) is not unique. Alternatively, one could handle this system by finding the associated eigenvalues and then utilizing them to obtain Eqs. (20) and (21). We direct the interested readers to Ref. [40] for a detailed description of this alternative method to solve systems of coupled first-order ODEs, as well as the physical interpretation of the eigenvalues. Furthermore, note that the authors of Ref. [43] have also utilized such alternative method to study the injection-driven instabilities arising in three-fluid flows.

Equations (20) and (21) describe the exponential time evolution of the perturbations growing (or decaying) in the inner and outer interfaces, respectively. From these relations, one obtains the time-dependent linear growth rates of the ferrofluid annular system,

$$\lambda_1(n, t) \equiv \frac{\dot{\zeta}_n}{\zeta_n} = f_1 \Lambda(n) + f_2 \Gamma(n) \frac{\varepsilon_n(t)}{\zeta_n(t)}, \quad (24)$$

and

$$\lambda_2(n, t) \equiv \frac{\dot{\varepsilon}_n}{\varepsilon_n} = f_3 \Lambda(n) \frac{\zeta_n(t)}{\varepsilon_n(t)} + f_4 \Gamma(n). \quad (25)$$

The linear equations (20), (21), (24), and (25) are not only necessary to assist the weakly nonlinear simulations presented in Sec. III, but also to provide essential linear stability information, such as the mode of largest growth rate n_{\max} , and also the phase velocities utilized to describe the rotational motion of the annular ferrofluid structures in Sec. IV.

In the next sections, we utilize the mode-coupling expressions (11) and (12) to study a variety of pattern morphologies acquired by the ferrofluid annulus subjected to the external

crossed magnetic fields arrangement, and to describe the corresponding dynamical behaviors at the onset of nonlinearities. Throughout the analysis of these important aspects of the problem, we ensure that all the dimensionless parameters (N_{Br} , N_{Ba} , R , and χ) considered in this work are consistent with realistic physical quantities related to existing experiments in confined ferrofluids in Hele-Shaw cell arrangements [28,31,34,45–48].

III. WEAKLY NONLINEAR FERROFLUID ANNULUS SHAPES

In this section, we take advantage of the flexibility offered by the crossed magnetic field configuration (independent manipulation of radial and azimuthal fields), and by the doubly connected nature of the ferrofluid annulus system (nontrivial coupling between inner and outer interfaces) to explore how the relative intensity of the radial and azimuthal magnetic field components (connected to the parameters N_{Br} , and N_{Ba}), and the thickness of the annular structure (related to the parameter R) affect the shape and dynamic behavior of the deformed, ring-shaped ferrofluid patterns.

The second-order, weakly nonlinear patterns exhibited in this work are all obtained by considering the coupling of $N = 40$ Fourier modes, namely the fundamental mode n , and its harmonics $2n, 3n, \dots$, and $40n$. This relatively large number of participating modes ($N = 40$) is utilized to ensure that the edges of the resulting fingering patterns are sufficiently smooth. We emphasize that we have performed repeated and careful computations utilizing more participating modes ($40 < N \leq 80$), and checked that the resulting findings (data and patterns) are indistinguishable from the results currently presented in this study. Throughout this work, we assume that the fundamental mode is given by the closest integer to the fastest growing mode at the final time $t = t_f$ of the evolution (i.e., the mode of maximum growth rate n_{\max}). Note that n_{\max} is obtained by evaluating the maximum of the real part of the linear growth rate, i.e., either

$$\left. \left\{ \frac{d}{dn} \text{Re}[\lambda_1(n, t = t_f)] \right\} \right|_{n=n_{\max}} = 0, \quad (26)$$

or

$$\left. \left\{ \frac{d}{dn} \text{Re}[\lambda_2(n, t = t_f)] \right\} \right|_{n=n_{\max}} = 0, \quad (27)$$

since the growth rates $\lambda_1(n, t)$ and $\lambda_2(n, t)$ very rapidly coincide for times much smaller than the final times t_f considered [39]. In this framing, we rewrite the complex interfacial perturbations $\zeta(\theta, t)$ [$\varepsilon(\theta, t)$] in terms of the real-valued cosine $a_n(t) = \zeta_n(t) + \zeta_{-n}(t)$ [$\bar{a}_n(t) = \varepsilon_n(t) + \varepsilon_{-n}(t)$], and sine $b_n(t) = i(\zeta_n(t) - \zeta_{-n}(t))$ [$\bar{b}_n(t) = i(\varepsilon_n(t) - \varepsilon_{-n}(t))$] amplitudes. Moreover, and without loss of generality, we set the phase of the fundamental mode so that $a_n > 0$, $\bar{a}_n > 0$, and take the initial conditions $a_n(0) = \bar{a}_n(0) = a_{2n}(0) = \bar{a}_{2n}(0) = \dots = a_{40n}(0) = \bar{a}_{40n}(0) = 10^{-5}$. Likewise, we consider that $b_n(0) = \bar{b}_n(0) = b_{2n}(0) = \bar{b}_{2n}(0) = \dots = b_{40n}(0) = \bar{b}_{40n}(0) = 0$. The time evolution of all these mode amplitudes is then obtained by numerically solving the corresponding coupled nonlinear differential equations, given by expressions (11) and (12).

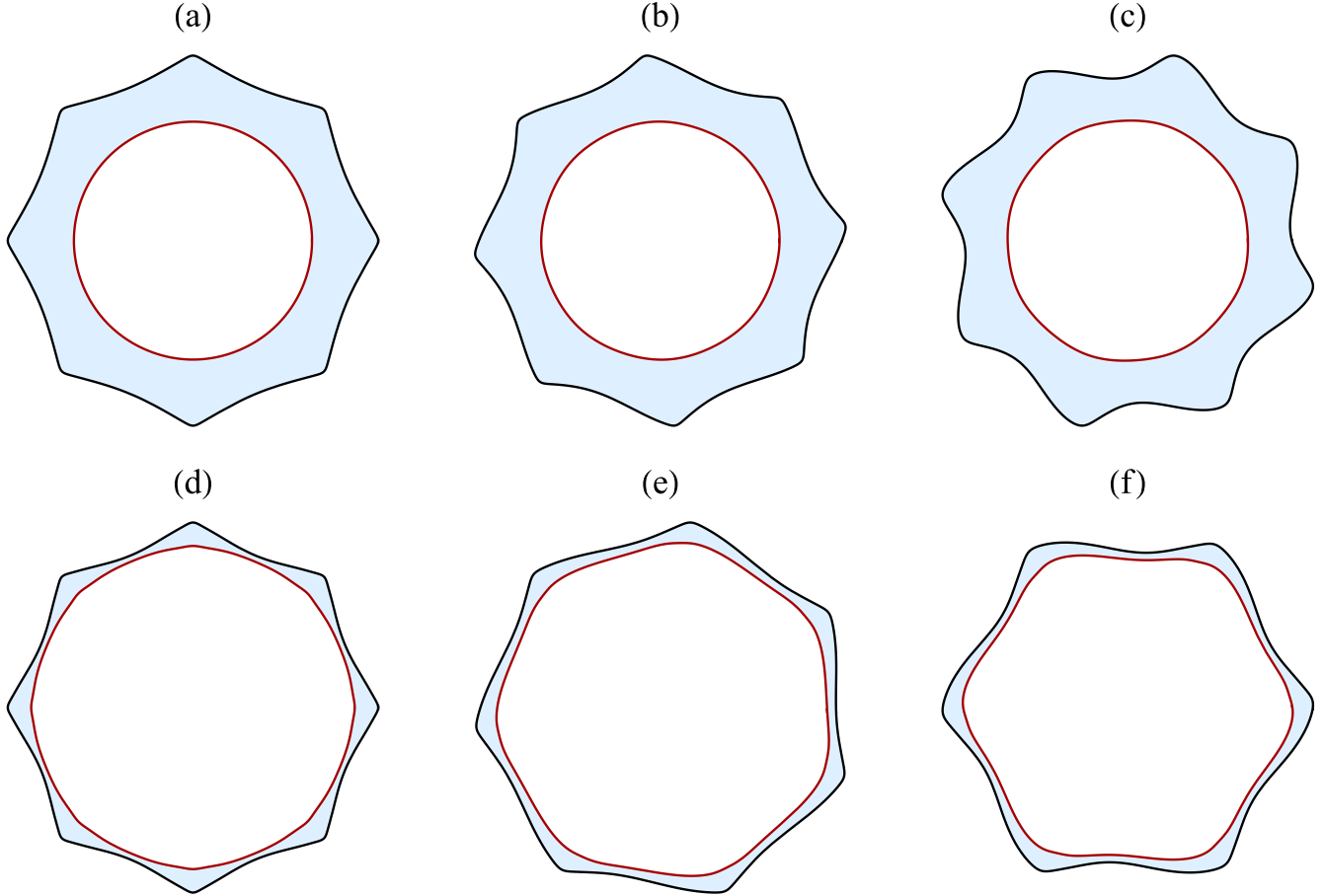


FIG. 2. Typical weakly nonlinear, annular ferrofluid patterns formed for a fixed radial magnetic Bond number $N_{Br} = 56$, and three increasing values of the azimuthal magnetic Bond number: $N_{Ba} = 0$ [(a) and (d)], $N_{Ba} = 4$ [(b) and (e)], and $N_{Ba} = 20$ [(c) and (f)]. In the top (bottom) panels we take $R = 0.70$ ($R = 0.94$). Moreover, we set $\chi = 1.5$, $R_2 = 1$, and final time $t_f = 0.03$. These patterns, and all others presented in this work, are plotted by considering the coupling of $N = 40$ ($n, 2n, 3n, \dots, 40n$) participating sine and cosine modes. The fundamental mode n is given by the closest integer to the fastest growing mode n_{max} evaluated at $t = t_f$. Here, we have that $n = n_{max} = 8$ [(a)–(d)], $n = n_{max} = 7$ (e), and $n = n_{max} = 6$ (f). In this figure, and throughout this study, we take $A_{12} = \mathcal{A} = 1$, $A_{23} = -1$, $\text{sgn}(I) = 1$, and $\sigma = 1$.

We begin our analysis by examining Fig. 2 which presents a series of representative weakly nonlinear ferrofluid annular patterns for the situation in which the radial magnetic Bond number is kept fixed at $N_{Br} = 56$, while the azimuthal magnetic Bond number assumes three increasingly larger values, namely $N_{Ba} = 0$ [Figs. 2(a) and 2(d)], $N_{Ba} = 4$ [Figs. 2(b) and 2(e)], and $N_{Ba} = 20$ [Figs. 2(c) and 2(f)]. This is done for two different values of the coupling strength parameter: $R = 0.70$ [Figs. 2(a)–2(c)] and $R = 0.94$ [Figs. 2(d)–2(f)]. With no loss of generality, in Fig. 2 and all remaining figures in this work, we consider the characteristic physical parameters $A_{12} = \mathcal{A} = 1$, $A_{23} = -1$, $\text{sgn}(I) = 1$, and $\sigma = 1$. In addition, for Fig. 2 we take $\chi = 1.5$, $R_2 = 1$, and final time $t_f = 0.03$.

Figures 2(a)–2(c) illustrate the impact of augmenting N_{Ba} (for fixed N_{Br}) on the shape and dynamic behavior of the annular ferrofluid patterns for the cases of thicker annuli, i.e., for a smaller value of R ($R = 0.70$). When $N_{Ba} = 0$ [Fig. 2(a)], one observes the formation of characteristic starlike, n -fold polygonal ferrofluid annular shape, with an outer interface presenting eight pointy fingers, accompanied by a fairly circular inner interface. This is exactly the kind of typical fluid

ring structure one detects when an initially slightly perturbed, thick ferrofluid ring is subjected solely to an applied radial field in a Hele-Shaw cell [39].

A more interesting scenario is unveiled in Fig. 2(b), when $N_{Br} = 56$ and $N_{Ba} = 4$: The combined action of radial and azimuthal magnetic fields results in the formation of a skewed annular ferrofluid pattern. Such a skewed structure still presents eight sharp fingers on its outer interface and a circular inner interface. Nevertheless, it is evident that the vertices of the eightfold polygonal annulus in Fig. 2(b) have positions that are different from those of the corresponding annulus portrayed in Fig. 2(a). Moreover, while in Fig. 2(a) the pointy finger profiles are quite symmetric, they are distorted and look a bit asymmetric in Fig. 2(b) due to the action of the nonzero azimuthal applied field. These findings for the ferrofluid annulus are consistent with similar results originally revealed in Ref. [37] and also observed in Ref. [38] for the corresponding simply connected situation in which a confined ferrofluid droplet is subjected to crossed, radial, and azimuthal magnetic fields. As discussed in Ref. [37], the magnetic traction term in the pressure jump boundary conditions [Eqs. (5)

and (6)] induces unequal normal stress on either side of the finger tip profile, breaking its symmetry and consequently leading to an increased skewness of the fingers. Therefore, by comparing Fig. 2(a) with Fig. 2(b) one verifies that the combined action of radial and azimuthal fields has two main effects on the annular patterns: (i) It changes a bit the position of the vertices of the pointy fingers [i.e., the pattern in Fig. 2(b) looks “rotated” with respect to the one shown in Fig. 2(a)] and (ii) breaks the original symmetry of the finger tips’ profiles exhibited in Fig. 2(a), creating skewed fingered structures in Fig. 2(b). Later in this work, we will see that the crossed magnetic fields can actually make the ferrofluid rings to rotate, without ever changing their forms (i.e., they reach stationary shapes).

Furthermore, by scrutinizing Fig. 2(c) for a larger azimuthal Bond number [$N_{Ba} = 20$] one finds the emergence of an even more deformed ferrofluid annular structure that, regardless of still having eight fingers, present protrusions that are larger and more skewed than the ones depicted in Fig. 2(b). Additionally, one can also see that the inner boundary of the ferrofluid ring in Fig. 2(c) is almost completely circular, exhibiting just a very modest deformation. Hence, from the behaviors revealed in Figs. 2(a)–2(c), one concludes that for thick ferrofluid annuli (i.e., for smaller values of R), the most appealing effects induced by the crossed magnetic fields are more clearly manifested at the outer boundary of the magnetic fluid annular patterns.

To explore the role played by the coupling strength parameter R , we continue our analysis by observing Figs. 2(d)–2(f) for which $R = 0.94$, resulting in the generation of ferrofluid annular structures that are thinner than those shown in Figs. 2(a)–2(c) for $R = 0.7$. As expected, larger values of R make the coupling between the inner and outer interfaces considerably stronger, revealing additional noteworthy aspects of the system. The most apparent effect of considering a larger R is that, in contrast to what occurred in Figs. 2(a)–2(c), in Figs. 2(d)–2(f) both the outer and the inner ferrofluid ring interfaces can be significantly impacted by the crossed magnetic fields. For instance, although the inner boundary is just mildly deformed when $N_{Ba} = 0$ [Fig. 2(d)], it becomes increasingly distorted as N_{Ba} is increased [Figs. 2(e) and 2(f)]. One can easily notice that the shape of the thin edges of the polygonal-like annular rings become progressively asymmetric and skewed as N_{Ba} is increased.

In addition to the degree of deformation of the annular fingered structures (finger skewness and asymmetry), another noticeable difference among the patterns on display in Figs. 2(a)–2(c) for $R = 0.70$ and in Figs. 2(d)–2(f) for $R = 0.94$ refers to the number of resulting fingers formed. Notice that for smaller R , one can increase the value of N_{Ba} , keeping the number of emerging fingers unchanged [all patterns in Figs. 2(a)–2(c) have eight fingers]. On the other hand, for larger R , by increasing N_{Ba} the number of generated fingers is decreased [in Figs. 2(d)–2(f) the patterns have eight, seven, and six fingers, respectively].

Similarly to what is discussed in the next paragraph regarding the degree of deformation of the annular ferrofluid shapes, as the magnitude of the azimuthal field is increased (for a fixed radial field) the number of produced fingers in the stationary, ring-shaped ferrofluid patterns is a result of

a complex nonlinear interplay between the outer and inner interfaces of the annulus. As exemplified in Fig. 2 (and also in Fig. 4), such a nonlinear response for the number of fingers is particularly dependent on the value of the coupling parameter R but also depends on all other relevant physical parameters of the problem (N_{Br} , N_{Ba} , χ , etc.). Unlike the simpler, two-fluid single-interface case, where one can obtain a closed-form expression for the number of fingers in terms of the physical parameters of the problem, in the current annular, double-interface system, such an expression cannot be found analytically. Therefore, precisely determining the general behavior for the number of resulting fingers arising in the *nonlinear, stationary-state* ferrofluid annular patterns under the influence of crossed magnetic fields is nontrivial.

At first glance, it may seem strange or contradictory that by increasing N_{Ba} in Fig. 2 one obtains more deformed ferrofluid annular patterns. After all, it is well known that, at the linear level, the azimuthal field tends to stabilize the outer interface (see Sec. II, and Ref. [30]). Therefore, from a purely linear perspective, by increasing N_{Ba} one would expect to get less deformed ferrofluid annular shapes, possibly having a decreased number of fingers. Moreover, as in Ref. [39], we have found that at the linear level the emerging patterns present fingers with rounded tips (no sharp fingers present), and skewness is completely absent. Obviously, this is not what is observed in Fig. 2. The justification for the behaviors disclosed in Fig. 2 is that such responses to the crossed magnetic fields are in fact due to complicated nonlinear coupling effects. One key ingredient responsible for the nonlinear behaviors detected in Fig. 2 is the magnetic traction term in the pressure boundary conditions [Eqs. (5) and (6)] which involves the coupling of N_{Br} and N_{Ba} . It turns out that such a term is intrinsically nonlinear [37,49] and has no influence at purely linear stages of interfacial evolution. As commented earlier, it is precisely this nonlinear magnetic traction term that induces the rising of the skewed fingers. Of course, as exemplified in Fig. 2, another very important contributor for the establishment of the nonlinear pattern formation phenomena in a ferrofluid annulus under crossed magnetic fields is the coupling parameter R . So, nonlinear effects do play an essential role to determine the pattern-forming behavior portrayed in Fig. 2. In summary, from the analysis of Fig. 2 we can say that, for a fixed N_{Br} , and by properly manipulating N_{Ba} , and R one can produce skewed, rotating ferrofluid, nonlinear annular patterns of different thicknesses and number of fingers, presenting variable degrees of deformation in both interfaces of the ferrofluid ring. Such a morphological and dynamical manageability of the ferrofluid annulus under crossed magnetic fields could be used as potential functionalities for a number of practical applications, as those discussed in Sec. I.

We close our discussion of the representative ferrofluid annular patterns presented in Fig. 2 by plotting in Fig. 3 the time evolution of the perturbation amplitudes for the inner interfaces $|\zeta_n(t)| = \sqrt{a_n^2(t) + b_n^2(t)}/2$ (dashed curves), as well as for the outer interfaces $|\varepsilon_n(t)| = \sqrt{\bar{a}_n^2(t) + \bar{b}_n^2(t)}/2$ (solid curves) associated with the situations resulting in the final time shapes shown in Fig. 2. For simplicity, in Fig. 3 we illustrate the general behavior of the mode amplitudes with time by focusing on the growth of a few representative modes which have sizable amplitudes. In this way, in Fig. 3 for

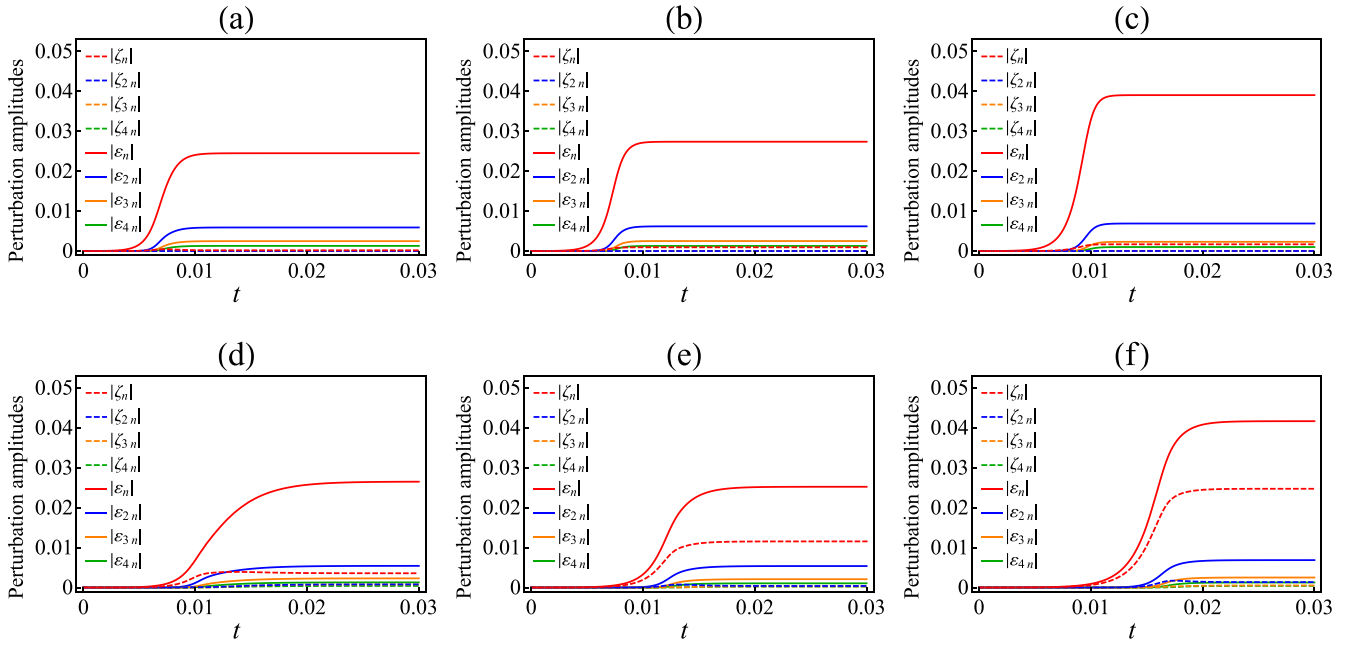


FIG. 3. Time evolution of the perturbation amplitudes of the inner $[|\zeta_n(t)| = \sqrt{a_n^2(t) + b_n^2(t)}/2]$ (dashed curves) and outer $[|\varepsilon_n(t)| = \sqrt{\bar{a}_n^2(t) + \bar{b}_n^2(t)}/2]$ interfaces, corresponding to the situations leading to the formation of the nonlinear annular ferrofluid structures displayed in Fig. 2. Amplitudes for modes n , $2n$, $3n$, and $4n$ are shown.

each case considered, we only plot curves for modes n , $2n$, $3n$, and $4n$. The curves for the smaller perturbation amplitudes of the remaining Fourier modes follow a similar trend of those explicitly displayed in Fig. 3, but all overlap close to the horizontal axes, being almost indistinguishable from one another. By observing the various curves in Fig. 3 one readily realizes that all of them present similar time evolution behaviors. Initially, at very early stages of the linear regime, after a latency time period for which the initially circular annular shape practically does not change, the curves start to grow exponentially. Then, at the weakly nonlinear regime, nonlinear effects take over, and the exponential growth of the linear instability does not proceed unchecked. As a consequence, after reaching a largest value, all the perturbation amplitudes saturate and remain unchanged as time progresses. This means that the second-order, nonlinear ferrofluid annulus shapes illustrated in Fig. 2 have reached a stationary-state configuration. As a matter of fact, as we will verify later (Sec. IV), the use of crossed radial and azimuthal magnetic fields leads to the formation of annular ferrofluid patterns which rotate with a controllable angular velocity but keeping stable permanent interfacial profiles. These particular features of the spinning ferrofluid ring structures under crossed magnetic fields in Hele-Shaw cells allow one to use it as an ideal laboratory system and as testing ground for a number of possible applications. For example, ring-shaped ferrofluid droplets could be used as shape-programmable magnetic fluid objects, which can move through narrow channels, transporting liquid samples and fragile objects, as well as acting as programmable fluidic-mixing devices in confined environments [19,20].

In order to further explore the great malleability of the ferrofluid annulus system under crossed magnetic field, we investigate a situation which is complementary to that

studied in Fig. 2, where the radial magnetic Bond number N_{Br} was kept fixed, while the azimuthal magnetic Bond number N_{Ba} was allowed to vary. Conversely, in Fig. 4 we examine what happens to the ferrofluid annular structures when N_{Ba} remains unmodified ($N_{Ba} = 100$), whereas three increasing values of the radial magnetic Bond number are utilized: $N_{Br} = 0$ [Figs. 4(a) and 4(d)], $N_{Br} = 14$ [Figs. 4(b) and 4(e)], and $N_{Br} = 50$ [Figs. 4(c) and 4(f)]. Moreover, we consider two different values of the coupling strength parameter: $R = 0.70$ [Figs. 4(a)–4(c)] and $R = 0.86$ [Figs. 4(d)–4(f)]. As in Fig. 2, we consider the typical parameters $A_{12} = \mathcal{A} = 1$, $A_{23} = -1$, and $\sigma = 1$. But in Fig. 4 we take $\chi = 0.9$, $R_1 = 0.7$, and final time $t_f = 0.04$.

First, we concentrate our attention on Figs. 4(a)–4(c) for the cases of thicker ferrofluid annuli ($R = 0.70$). Now, when N_{Ba} is fixed, and N_{Br} is increased, in contrast to what we have seen in Figs. 2(a)–2(c), the inner interfaces of the annuli are the ones that deform the most, while the outer boundaries retain their circular shape. When $N_{Br} = 0$ [Fig. 4(a)] one observes the formation of a sixfold polygonal-like inner interface, having pointy vertices and edges that are almost straight. However, as N_{Br} assumes nonzero values [Figs. 4(b) and 4(c)], we notice that the edges of the still hexagonal inner interfaces start to curve and distort, becoming increasingly asymmetric for higher values of N_{Br} . From Figs. 4(a)–4(c) one observes that by augmenting N_{Br} the positions of the vertices are modified, apparently indicating a rotation of the skewed annular structures in the clockwise direction. It is worthwhile to note that, by contrast, the structures shown in Fig. 2 turned in the opposite (counterclockwise) direction.

At this point, we examine the cases of thinner ferrofluid annuli ($R = 0.86$) [Figs. 4(d)–4(f)]. Recall that higher values of R imply in a stronger coupling between the inner and outer interfaces. So, depending on the values of N_{Br} ,

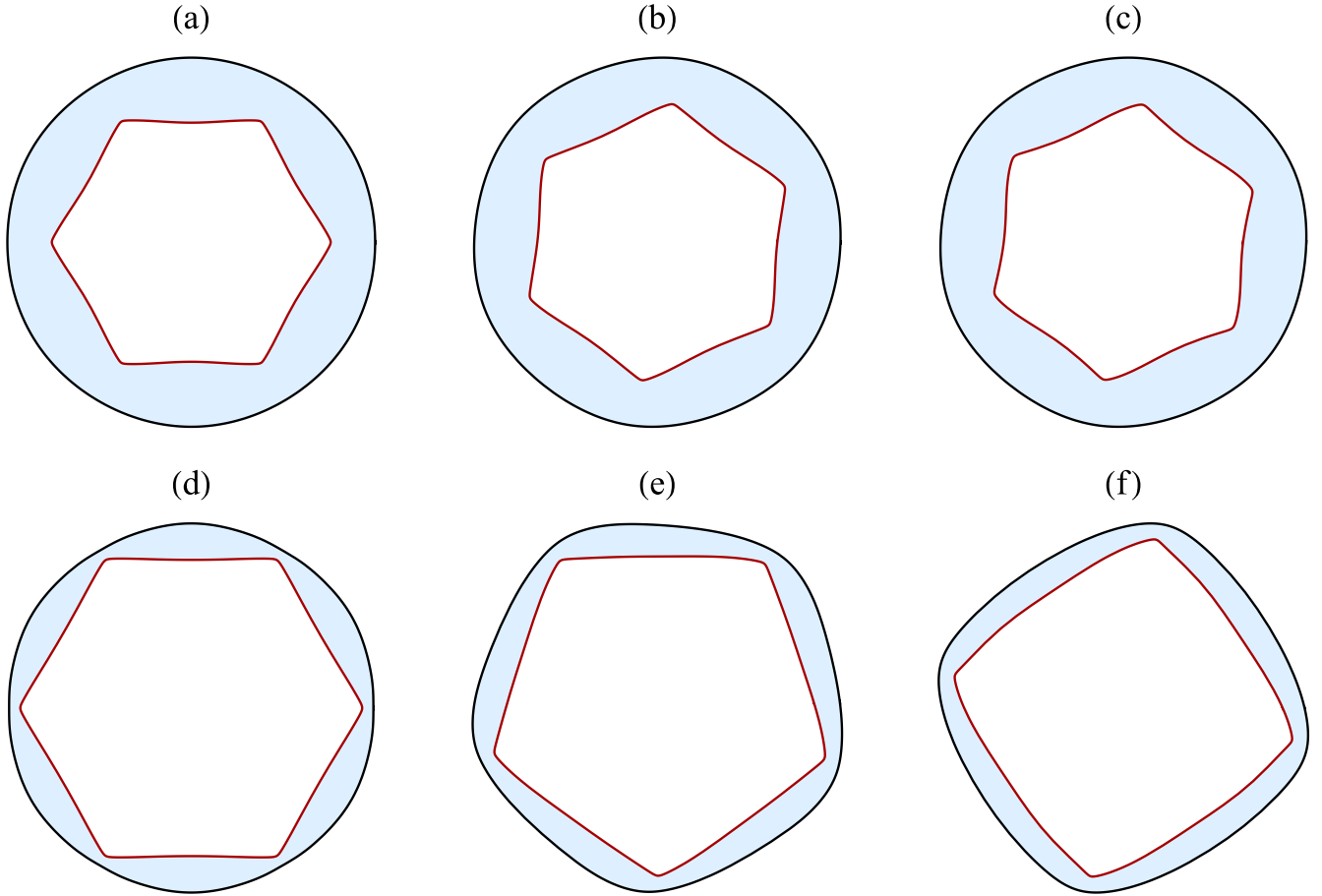


FIG. 4. Representative weakly nonlinear, annular ferrofluid patterns formed for a constant azimuthal magnetic Bond number $N_{Ba} = 100$, and three increasing values of the radial magnetic Bond number: $N_{Br} = 0$ [(a) and (d)], $N_{Br} = 14$ [(b) and (e)], and $N_{Br} = 50$ [(c) and (f)]. In the top (bottom) panels we take $R = 0.70$ ($R = 0.86$). In addition, we set $\chi = 0.9$, $R_1 = 0.7$, and final time $t_f = 0.04$. Here we have that $n = n_{max} = 6$ [(a)–(d)], $n = n_{max} = 5$ (e), and $n = n_{max} = 4$ (f). The remaining physical parameters, initial conditions, and the number of participating modes are the same as those used in Fig. 2.

one could get perturbed ferrofluid ring shapes having both boundaries (inner and outer) significantly deformed. When $N_{Br} = 0$ [Fig. 4(d)] we see the emergence of a thin annular structure having an inner interface in the form of an almost perfect regular hexagon with straight edges, and symmetric finger profiles at the vertices, surrounded by an almost circular outer boundary. Nevertheless, when $N_{Br} = 14$ [Fig. 4(e)] something different emerges: Now we have the formation of a pentagonal inner interface having slightly skewed fingers and weakly asymmetric edges, involved by a gently deformed, fivefold symmetric outer interface. On the other hand, if the radial Bond number is even larger, as in Fig. 4(f) ($N_{Br} = 50$), then one finds the formation of an annular structure having a fourfold symmetric inner boundary, presenting more intensively skewed fingers and a bit more asymmetric edges. Due to the strong interface coupling, the outer interface follows the inner one and also assumes a fourfold, squarelike shape.

It is worthwhile to note that, as in the ferrofluid annulus cases discussed in Figs. 2 and 3, the magnetic fluid annular patterns illustrated in Fig. 4 are also stationary states. This is demonstrated in Fig. 5 which presents the time evolution of perturbation amplitudes for the inner (dashed curves) and

outer (solid curves) interfaces of the annular ferrofluid structures pictured in Fig. 4.

From our discussion of Figs. 2–5 we conclude that, by properly manipulating the magnetic Bond numbers N_{Ba} and N_{Br} , one has a myriad of possibilities of creating and controlling a number of nonlinear ferrofluid ring structures having different thicknesses and distinct levels of finger skewness, asymmetry, and sharpness.

IV. ROTATIONAL MOTION OF THE FERROFLUID ANNULUS

In Figs. 2(b), 2(c), 2(e), and 2(f), we have identified the formation of ferrofluid annular structures under crossed magnetic field setup ($N_{Br} \neq 0$ and $N_{Ba} \neq 0$) that seem rotated when compared with their counterparts [Figs. 2(a) and 2(d)] generated for a purely radial magnetic field ($N_{Br} \neq 0$ and $N_{Ba} = 0$). For instance, the motionless annular patterns displayed in Figs. 2(a) and 2(d) clearly exhibit a finger protuberance at the uppermost portions of these structures. However, no fingers are found at these locations in the patterns shown in Figs. 2(c) and 2(f). Instead, we observe undulated edges, and therefore this fact indicates that not only these patterns, but

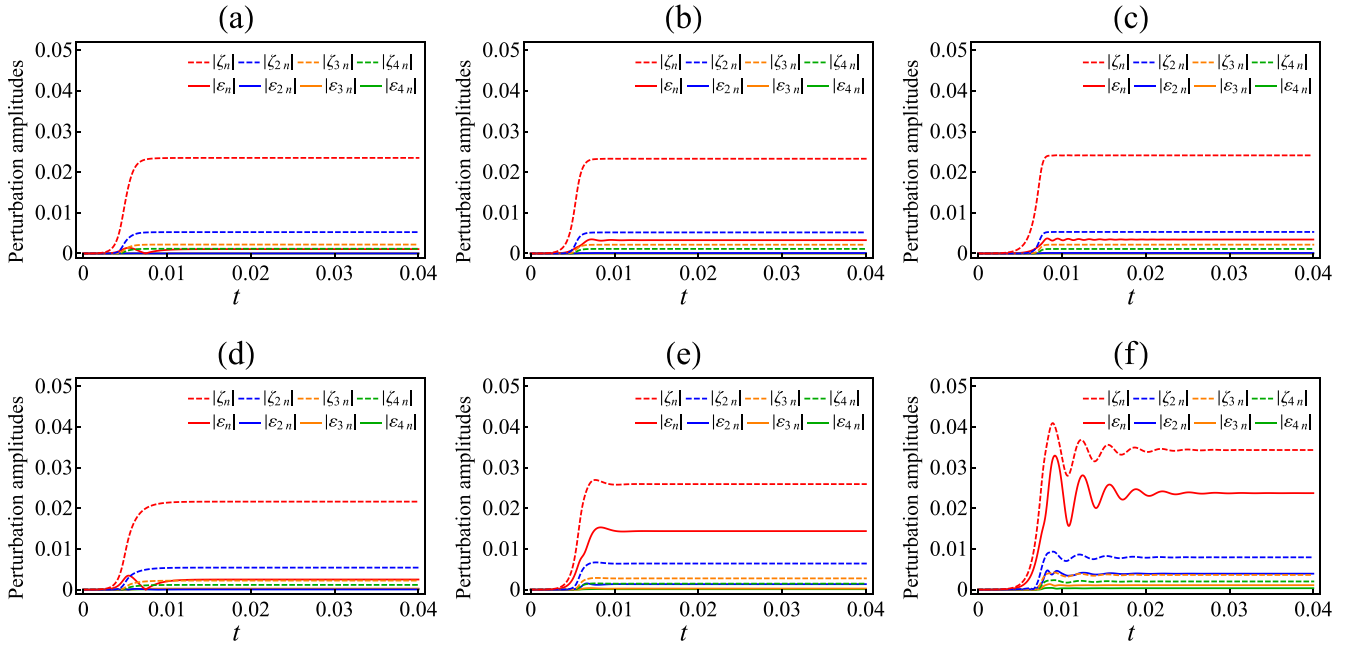


FIG. 5. Time evolution of the perturbation amplitudes of the inner $[\zeta_n(t)] = \sqrt{a_n^2(t) + b_n^2(t)}/2]$ (dashed curves) and outer $[\varepsilon_n(t)] = \sqrt{\bar{a}_n^2(t) + \bar{b}_n^2(t)}/2]$ boundaries of the ferrofluid ring, corresponding to the situations resulting in the nonlinear annular patterns depicted in Fig. 4. Amplitudes for modes $n, 2n, 3n,$ and $4n$ are shown.

all the other annular structures generated considering $N_{Br} \neq 0$ and $N_{Ba} \neq 0$ rotate with respect to the structures obtained for $N_{Br} \neq 0$ and $N_{Ba} = 0$. Additionally, this happens regardless of the value of the coupling strength parameter R . A similar phenomenon is observed in the patterns presented in Fig. 4.

In order to investigate the rotational motion of the annular patterns under crossed magnetic fields observed in Figs. 2 and 4, in Fig. 6(a) [Fig. 6(b)] we depict superposed snapshots taken at times $t = 3.02 \times 10^{-2}$, $t = 3.04 \times 10^{-2}$, and $t = 3.05 \times 10^{-2}$ [$t = 4.29 \times 10^{-2}$, $t = 4.31 \times 10^{-2}$, and $t =$

4.33×10^{-2}] of the pattern originally displayed in Fig. 2(c) [Fig. 4(c)]. By analyzing the snapshots displayed in Fig. 6(a), it is evident that, as time increases, the annular structure rotates in the counterclockwise direction (as indicated by the curly black arrow). Something analogous is also detected in Fig. 6(b). However, in Fig. 6(b) the rotational motion exhibited by the ring-shaped pattern occurs in the opposite direction, i.e., in the clockwise sense. Note that both annular structures depicted in Figs. 6(a) and 6(b) rotate while preserving their shape profiles, which is in agreement with their

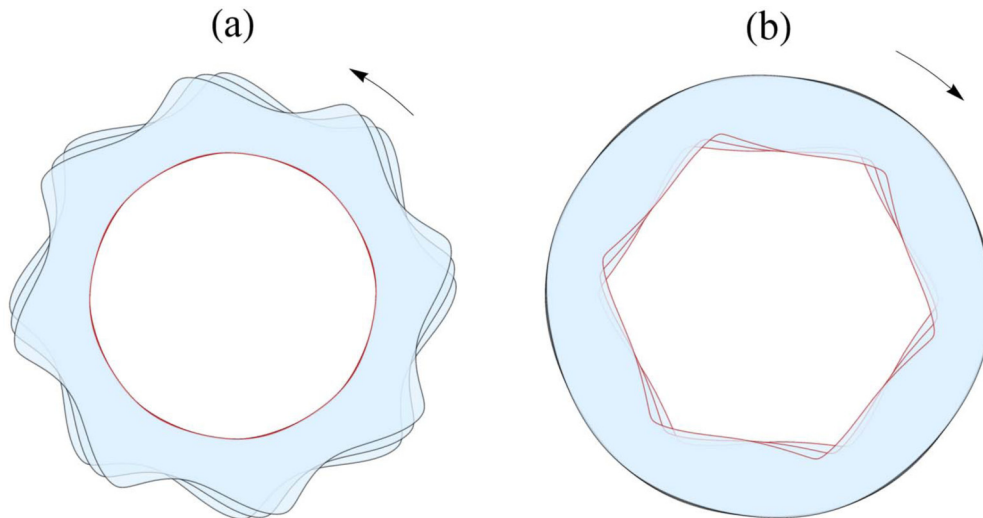


FIG. 6. (a) Overlaid snapshots of the pattern investigated in Fig. 2(c), taken at times $t = 3.02 \times 10^{-2}$, $t = 3.04 \times 10^{-2}$, and $t = 3.05 \times 10^{-2}$, illustrating a counterclockwise rotational motion of the ferrofluid annulus. Likewise, (b) displays superposed snapshots of the pattern examined in Fig. 4(c), shown at times $t = 2.29 \times 10^{-2}$, $t = 2.31 \times 10^{-2}$, and $t = 2.33 \times 10^{-2}$, exhibiting a clockwise spin of the ferrofluid ring. The curly black arrows indicate the directions of rotation.

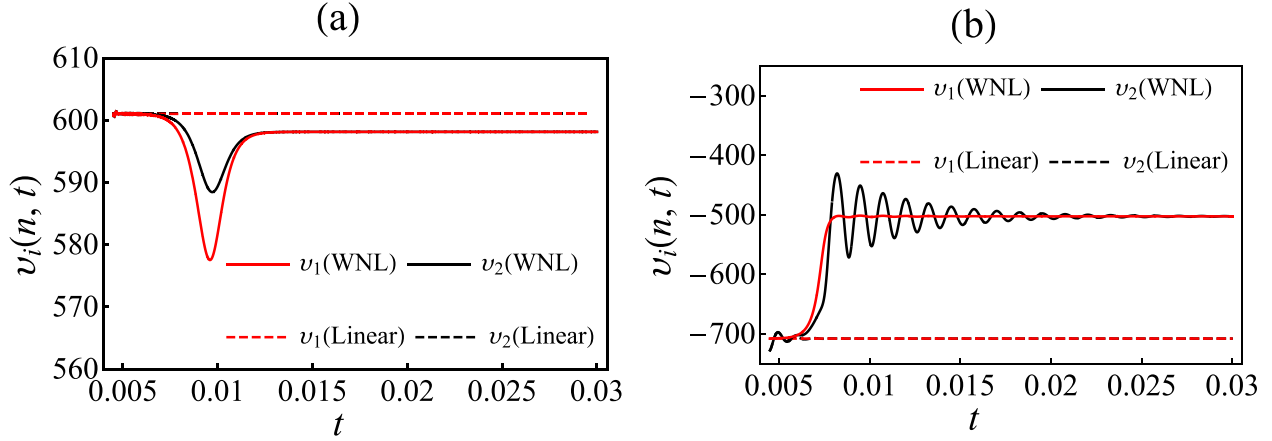


FIG. 7. Linear (dashed) and weakly nonlinear (solid) phase velocities $v_i(n, t)$ with $i = 1, 2$, and $n = n_{\max}$, as a function of time t for the time evolution of the annular ferrofluid patterns portrayed in (a) Fig. 6(a) and (b) Fig. 6(b).

corresponding saturated perturbation amplitudes observed in Fig. 3(c) and Fig. 5(c), respectively.

This sort of magnetically induced rotational motion was already observed previously in works addressing the problem of confined ferrofluid droplets under crossed magnetic fields [37,38], and as proposed in Ref. [37], the motion is caused by a force imbalance coming from the magnetic normal traction, which breaks the symmetry of the droplet when subjected to the two-component magnetic field. Nonetheless, in the two-fluid, single-interface, simply connected system studied in Refs. [37,38], the rotational motion can only occur in the counterclockwise direction, unless one modifies the electric current's direction passing through the wire generating the azimuthal magnetic field component. Alternatively, one could change the fluids' positions, i.e., consider a nonmagnetic fluid droplet surrounded by a ferrofluid. On the other hand, in three-fluid, two-interface, doubly connected system examined here, we are able to manipulate the ring-shaped patterns' direction of rotation by only altering the relative intensity of radial (N_{Br}) and azimuthal (N_{Ba}) magnetic field components, while keeping the electric current's direction and fluids' position fixed. Moreover, we have verified that the direction of rotation of the annular patterns follows the original motion of the interface with the largest overall perturbation. That is, if for a given set of parameters N_{Br} , N_{Ba} , and $R \neq 0$, then the outer interface is more disturbed than the inner one, then the annular structure rotates in the counterclockwise direction. This is the case for all the patterns exhibited in Fig. 2 for which $N_{Br} \neq 0$ and $N_{Ba} \neq 0$. Conversely, if the inner interface is more perturbed than the outer one, then the whole structure rotates in the clockwise direction, and this is the situation illustrated in Fig. 4 whenever $N_{Br} \neq 0$ and $N_{Ba} \neq 0$.

The visual conclusions obtained in Fig. 6 are quantitatively supported by the complementary results presented in Fig. 7, where we plot the linear (dashed curves) and weakly nonlinear (solid curves) phase velocities $v_i(n, t)$, with $i = 1$ ($i = 2$) for the inner (outer) interface, as a function of time t . Figure 7(a) [Fig. 7(b)] represents the phase velocities corresponding to the rotating annular structure displayed in Fig. 6(a) [Fig. 6(b)], with $n = n_{\max} = 8$ [$n = n_{\max} = 6$]. The linear curves of $v_i(n, t)$, i.e., v_i (linear), are obtained

by evaluating $-\text{Im}[\lambda_i(n, t)]/n$ with the help of Eqs. (24) and (25). Additionally, the weakly nonlinear predictions for $v_i(n, t)$, i.e., v_i (WNL), are obtained by numerically evaluating $-\text{Im}[\zeta_n(t)/\zeta_n(t)]/n$ (for $i = 1$) and $-\text{Im}[\dot{\epsilon}_n(t)/\epsilon_n(t)]/n$ (for $i = 2$) with the assistance of Eqs. (11) and (12), respectively. We call the readers attention to not confuse the time-dependent, coupled phase velocities $v_i(n, t)$ examined here with the time-independent, decoupled velocities $V_i(n)$ presented in Sec. II when we discussed the two-fluid, single-interface limit.

We initiate our analysis of Fig. 7 by discussing the linear predictions for $v_i(n, t)$ depicted in Fig. 7(a). It is evident that the two dashed curves overlap, in addition of being positive, and constant in time. Therefore, linear theory predicts that the annular ferrofluid pattern rotates in the counterclockwise direction with constant angular velocity during the whole dynamics. The linear theory indeed captures the correct direction of rotation of the annular pattern, but it is not accurate in predicting the magnitude of the angular velocity, and the dynamics of this rotational motion, as we notice by comparing the linear and WNL curves. By following the behaviors of v_i (WNL), we observe that for early times, when the perturbation amplitudes on both interfaces are very small and nonlinear effects are negligible, WNL and linear predictions for the phase velocities are practically the same. Nevertheless, as time progresses, the perturbation amplitudes become larger and nonlinear effects start to impact the dynamics of the rotational motion by reducing the magnitude of the phase velocities $v_i(n, t)$. Later, after a short transient, the v_i (WNL) curves saturate at a value of phase velocity that is about 0.5% smaller than the magnitude predicted by v_i (linear). We have verified similar reductions of about 6.4% in the case portrayed in Fig. 2(b) and of 14.1% in Fig. 2(e). Actually, we have also found a small increase of about 2.6% in Fig. 2(f) but only for these particularly higher values of N_{Br} and R . Therefore, our second-order mode-coupling theory provides a weakly nonlinear correction to the linear prediction of the propagation velocity. Our findings reinforce the importance of developing a nonlinear theory for this annular system since a purely linear theory cannot accurately describe either the annular pattern-formation process or rotational motion dynamics. It is worth

noting that similar weakly nonlinear corrections have also been found in related ferrohydrodynamic problems studied in Refs. [50,51], where researchers investigated the generation of nonlinear waves on ferrofluid interfaces in rectangular Hele-Shaw cells under an in-plane tilted, externally applied magnetic field which makes an arbitrary angle with an initially unperturbed ferrofluid interface.

We conclude our discussion regarding the rotational dynamics of the ferrofluid annulus under crossed magnetic fields by inspecting Fig. 7(b). Note that all the conclusions obtained previously in Fig. 7(a) about the rotational dynamics, and the linear and weakly nonlinear predictions for this motion, remain valid for the case illustrated in Fig. 7(b). For example, in Fig. 7(b) one also detects a weakly nonlinear correction to the linear prediction of the propagation velocity: In this case, the v_i (WNL) curves saturate at a value that is about 29% smaller than the magnitude predicted by v_i (linear). The related reductions in the other relevant cases in Fig. 4 are 29.9% in Fig. 4(b), 49% in Fig. 4(e), and 30.2% in Fig. 4(f). A few additional remarks are still worth mentioning in Fig. 7(b): First, note that now all the curves, regardless of being linear or WNL, are associated to negative values of the phase velocities. This implies a rotational motion in the clockwise direction, in agreement with the rotation of the annular structure displayed in Fig. 6(b). Furthermore, we observe that v_1 (WNL) reaches a saturated value of about -500 very quickly, while v_2 (WNL) follows a similar trend but oscillating around that value before saturating at a later time. Analogous oscillatory behaviors of phase velocities were also identified previously in Refs. [37,51], and they are connected to meaningless transients occurring before the establishment of the permanent annular shape profile.

We have also examined the rotational dynamics utilizing values of dimensionless parameters beyond those considered in Fig. 7, and our main findings can be summarized as follows: For all the weakly nonlinear simulations performed, we noticed that the magnitude of the phase velocities increases when either larger values of N_{Br} or N_{Ba} are utilized. This increase in the phase velocities v_i of the coupled system (i.e., for $R \neq 0$) for larger values of N_{Br} and N_{Ba} is indeed expected, since the linear phase velocities V_i of the fully decoupled system (i.e., for $R \rightarrow 0$) presented in Sec. II are proportional to $\sqrt{N_{Br}N_{Ba}}$. In addition, R controls the time required for v_1 (WNL) and v_2 (WNL) match together at the final saturated magnitude, being that time is larger for smaller values of R .

V. CONCLUDING REMARKS

We have investigated the problem of the immiscible displacement of an intermediate annular layer of a ferrofluid, bounded by nonmagnetic fluids in the confined geometry of a Hele-Shaw cell. Such a dual-interface ferrofluid system is under the influence of crossed magnetic fields, having radial and azimuthal components. This particular ferrohydrodynamic setup is of special interest since (i) it involves the interplay between two disjoint interfaces of a doubly connected magnetic fluid region and (ii) permits separate bidirectional magnetic manipulation (via radial and azimuthal field components) of the inner and outer boundaries of the ferrofluid ring.

Our second-order mode-coupling analysis reveals the emergence of a family of nonlinear, stationary pattern-forming structures. After an initial linear stage of exponential growth, nonlinear effects become important, and the ferrofluid annulus deforms, giving rise to skewed fingered protrusions. These fingers eventually cease to grow and reach a permanent profile. Furthermore, due to the action of the crossed magnetic fields, such immutable-shaped patterns rotate with a predetermined angular velocity, whose magnitude and direction can be regulated by the relative strength between the radial and azimuthal components of the applied magnetic field.

We have found that the thickness of the annulus also plays a key role in determining the nonlinear shape of the annular ferrofluid structure, with thinner annuli presenting enhanced coupling between the outer and inner boundaries of the magnetic fluid ring. One particularly interesting feature of the magnetic fluid annular configuration under crossed fields is the fact that, depending on the magnitude of the fields' components and the thickness of the ferrofluid ring, the two bounding interfaces can be made simultaneously unstable. Moreover, we have verified that the number of fingers produced can be tuned by the external magnetic field. Finally, our second-order mode-coupling analysis provides a correction to the linear prediction of the angular velocity, indicating that for the most cases studied, the weakly nonlinear coupling between the various interfacial modes leads to a reduced value of the spinning velocity.

As discussed in Sec. I, magnetically controlled annular ferrofluid systems offer a number of possibilities for microscale applications and fluid flow manipulation in confined environments. Considering the specific findings of our current study, the rotating ring-shaped ferrofluid droplets we studied could be used to provide efficient fluid mixing at low Reynolds numbers in narrow channels. Mixing under such circumstances is challenging, since one normally cannot rely on either turbulence or inertial effects to produce disorder in the velocity field. Another possible capability for ferrofluid annuli structures is to utilize their magnetic controllability, shape malleability, and intrinsic doubly connected nature in on demand liquid-cargo delivery functions, since they could trap, transport, and release liquid samples and delicate objects in an efficacious manner.

A natural extension of this work consists in examining the pattern-forming dynamics of the dual-interface ferrofluid structures under crossed magnetic fields during advanced times through fully nonlinear numerical simulations. We plan to perform such a challenging numerical study in the future, with the generalization of available boundary integral approaches via the vortex-sheet formulation [38] to doubly connected ferrofluid regions. Another stimulating possibility is to study theoretically the corresponding behavior of a confined magnetorheological (MR) fluid [52,53] annulus under the influence of applied crossed magnetic fields, where in addition to the issues discussed in this work, one could consider how the magnetically induced yield-stress effects of MR fluids would affect the system. Finally, we hope that experimentalists will feel motivated to verify the theoretical pattern-forming predictions presented in this work.

ACKNOWLEDGMENTS

J.A.M. thanks Conselho Nacional de Desenvolvimento Científico e Tecnológico for financial support under Grant No. 305140/2019-1. We are indebted to Írio M. Coutinho and Rodolfo Brandão for valuable discussions and helpful comments.

APPENDIX : SECOND-ORDER MODE-COUPLING FUNCTIONS

This Appendix presents the expressions for the second-order mode-coupling functions which appear in the text.

In Eq. (11), the second-order terms are given by

$$F(n, n') = -\frac{\mathcal{A}|n|}{R_1} \left\{ \frac{\sigma}{R_1^3} \left[1 - \frac{n'}{2}(3n' + n) \right] + \frac{\chi}{2} \left[(1 + \chi)N_{\text{Br}} + 3\frac{N_{\text{Ba}}}{R_1^4} + \chi \left(N_{\text{Br}} - \frac{N_{\text{Ba}}}{R_1^4} \right) n'(n - n') \right] + in' \chi^2 \text{sgn}(I) \frac{\sqrt{N_{\text{Ba}}N_{\text{Br}}}}{R_1^2} \right\}, \quad (\text{A1})$$

$$G(n, n') = \frac{1}{R_1} \{ A_{12}|n|[1 - g_1(n, n') \text{sgn}(nn')] - f_1^{-1} \}, \quad (\text{A2})$$

$$H(n, n') = -\frac{|n|}{R_2} \left\{ \frac{1}{R_2^3} \left[1 - \frac{n'}{2}(3n' + n) \right] - \frac{\chi}{2} \left[(1 + \chi)N_{\text{Br}} + 3\frac{N_{\text{Ba}}}{R_2^4} + \chi \left(N_{\text{Br}} - \frac{N_{\text{Ba}}}{R_2^4} \right) n'(n - n') \right] - in' \chi^2 \text{sgn}(I) \frac{\sqrt{N_{\text{Ba}}N_{\text{Br}}}}{R_2^2} \right\}, \quad (\text{A3})$$

$$I(n, n') = \frac{1}{R_2} \{ A_{23}|n|[1 - g_2(n') \text{sgn}(nn')] \}, \quad (\text{A4})$$

$$J(n, n') = \frac{|n|}{R_1} \left\{ \frac{(A_{23} + 1)R^{|n|+2}}{1 - R^{2|n|}} \text{sgn}(nn') \right\}, \quad (\text{A5})$$

$$K(n, n') = \frac{|n|}{R_1} \left\{ \frac{(A_{23}R^{2|n|} + 1)R^{|n|-|n'|}}{1 - R^{2|n'|}} \text{sgn}(nn') \right\}, \quad (\text{A6})$$

where

$$g_1(n, n') = \left(\frac{A_{12} + 1}{2A_{12}} \right) \frac{(1 + A_{23}R^{2|n|})(1 + R^{2|n'|})}{(1 - A_{23}R^{2|n|})(1 - R^{2|n'|})} + \left(\frac{A_{12} - 1}{2A_{12}} \right), \quad (\text{A7})$$

$$g_2(n') = \frac{A_{23} + 1}{A_{23}(1 - R^{2|n'|})}, \quad (\text{A8})$$

and the sgn function equals ± 1 according to the sign of its argument.

The second-order expressions in Eq. (12) are given by

$$\mathcal{F}(n, n') = H(n, n'), \quad (\text{A9})$$

$$\mathcal{G}(n, n') = \frac{1}{R_2} \{ A_{23}|n|[1 - g_3(n, n') \text{sgn}(nn')] - f_4^{-1} \}, \quad (\text{A10})$$

$$\mathcal{H}(n, n') = F(n, n'), \quad (\text{A11})$$

$$\mathcal{I}(n, n') = \frac{1}{R_1} \{ A_{12}|n|[1 - g_4(n') \text{sgn}(nn')] \}, \quad (\text{A12})$$

$$\mathcal{J}(n, n') = \frac{|n|}{R_2} \left\{ \frac{(A_{12} - 1)R^{|n|-2}}{1 - R^{2|n'|}} \text{sgn}(nn') \right\}, \quad (\text{A13})$$

$$\mathcal{K}(n, n') = \frac{|n|}{R_2} \left\{ \frac{(A_{12}R^{2|n|} - 1)R^{|n|-|n'|}}{1 - R^{2|n'|}} \times \text{sgn}(nn') \right\}, \quad (\text{A14})$$

where

$$g_3(n') = \left(\frac{A_{23} - 1}{2A_{23}} \right) \frac{(1 - A_{12}R^{2|n|})(1 + R^{2|n'|})}{(1 + A_{12}R^{2|n|})(1 - R^{2|n'|})} + \left(\frac{A_{23} + 1}{2A_{23}} \right), \quad (\text{A15})$$

and

$$g_4(n') = \frac{A_{12} - 1}{A_{12}(1 - R^{2|n'|})}. \quad (\text{A16})$$

-
- [1] R. E. Rosensweig, *Ferrohydrodynamics* (Cambridge University Press, Cambridge, UK, 1985).
- [2] E. Blums, A. Cebers, and M. M. Maiorov, *Magnetic Fluids* (de Gruyter, New York, 1997).
- [3] B. M. Berkovsky and V. Bashtovoy, *Magnetic Fluids and Applications Handbook* (Begell House, NY, 1996).
- [4] J.-C. Bacri, R. Perzynski, and D. Salin, Magnetic liquids, *Endeavour* **12**, 76 (1988).
- [5] I. Torres-Díaz, and C. Rinaldi, Recent progress in ferrofluids research: Novel applications of magnetically controllable and tunable fluids, *Soft Matter* **10**, 8584 (2014).
- [6] S. Afkhami and Y. Renardy, Ferrofluids and magnetically guided superparamagnetic particles in flows: A review of simulations and modeling, *J. Eng. Math.* **107**, 231 (2017).
- [7] X. Zhang, L. Sun, Y. Yu, and Y. Zhao, Flexible ferrofluids: Design and applications, *Adv. Mater.* **31**, 1903497 (2019).
- [8] M. Kole and S. Khandekar, Engineering applications of ferrofluids: A review, *J. Mag. Mag. Mat.* **537**, 168222 (2021).
- [9] W. Wang *et al.*, Multifunctional ferrofluid-infused surfaces with reconfigurable multiscale topography, *Nature (Lond.)* **559**, 77 (2018).

- [10] Q. Pankhurst, N. Thanh, S. Jones, and J. Dobson, Progress in applications of magnetic nanoparticles in biomedicine, *J. Phys. D* **42**, 224001 (2009).
- [11] L. Kafrouni and O. Savadogo, Recent progress on magnetic nanoparticles for magnetic hyperthermia, *Prog. Biomater.* **5**, 147 (2016).
- [12] S. Douezan, K. Guevorkian, R. Naouar, S. Dufour, D. Cuvelier, and F. Brochard-Wyart, Spreading dynamics and wetting transition of cellular aggregates, *Proc. Natl. Acad. Sci. USA* **108**, 7315 (2011).
- [13] G. Frasca, V. Du, J.-C. Bacri, F. Gazeau, C. Gay, and C. Wilhelm, Magnetically shaped cell aggregates: From granular to contractile materials, *Soft Matter* **10**, 5045 (2014).
- [14] F. Serwane, A. Mongera, P. Rowghanian, D. A. Kealhofer, A. A. Lucio, Z. M. Hockenbery, and O. Campàs, In vivo quantification of spatially-varying mechanical properties in developing tissues, *Nat. Methods* **14**, 181 (2017).
- [15] R. Seemann, M. Brinkmann, T. Pfohl, and S. Herminghaus, Droplet based microfluidics, *Rep. Prog. Phys.* **75**, 016601 (2012).
- [16] Y. Zhang and N.-T. Nguyen, Magnetic digital microfluidics—A review, *Lab Chip* **17**, 994 (2017).
- [17] W. Yu *et al.*, A ferrobotic system for automated microfluidic logistics, *Sci. Robot.* **5**, eaba4411 (2020).
- [18] A. Li *et al.*, Programmable droplet manipulation by a magnetic-actuated robot, *Sci. Adv.* **6**, eaay5808 (2020).
- [19] X. Fan, X. Dong, A. C. Karacakol, H. Xie, and M. Sitti, Reconfigurable multifunctional ferrofluid droplet robots, *Proc. Natl. Acad. Sci. USA* **117**, 27916 (2020).
- [20] V. Nasirimarekani, F. Benito-Lopez, and L. Basabe-Desmonts, Tunable superparamagnetic ring (tSPRing) for droplet manipulation, *Adv. Funct. Mater.* **31**, 2100178 (2021).
- [21] D. Andelman and R. E. Rosensweig, Modulated phases: Review and recent results, *J. Phys. Chem. B* **113**, 3785 (2009).
- [22] J.-C. Bacri and F. Elias, in *Morphogenesis: Origins of Patterns and Shapes*, edited by P. Bourguin and A. Lesne (Springer, New York, 2011).
- [23] A. Zakinyan, E. Beketova, and Y. Dikansky, Flows and instabilities of ferrofluids at the microscale, *Microfluid. Nanofluid.* **21**, 88 (2017).
- [24] P. G. Saffman and G. I. Taylor, The penetration of a fluid into a porous medium or Hele-Shaw cell containing a more viscous liquid, *Proc. R. Soc. Lond. A* **245**, 312 (1958).
- [25] For review papers on this topic, see D. Bensimon, L. P. Kadanoff, S. Liang, B. I. Shraiman, and C. Tang, Viscous flows in two dimensions, *Rev. Mod. Phys.* **58**, 977 (1986); G. M. Homsy, Viscous fingering in porous media, *Annu. Rev. Fluid Mech.* **19**, 271 (1987); K. V. McCloud and J. V. Maher, Experimental perturbations to Saffman-Taylor flow, *Phys. Rep.* **260**, 139 (1995); J. Casademunt, Viscous fingering as a paradigm of interfacial pattern formation: Recent results and new challenges, *Chaos* **14**, 809 (2004).
- [26] A. Cebers and M. M. Maiorov, Magnetostatic instabilities in plane layers of magnetizable liquids, *Magneto hydrodynamics (NY)* **16**, 21 (1980).
- [27] A. Cebers, Dynamics of magnetostatic instabilities, *Magneto hydrodynamics (NY)* **17**, 113 (1981).
- [28] D. P. Jackson, R. E. Goldstein, and A. O. Cebers, Hydrodynamics of fingering instabilities in dipolar fluids, *Phys. Rev. E* **50**, 298 (1994).
- [29] J. Kent-Dobias and A. J. Bernoff, Energy-driven pattern formation in planar dipole-dipole systems in the presence of weak noise, *Phys. Rev. E* **91**, 032919 (2015).
- [30] J. A. Miranda, Rotating Hele-Shaw cells with ferrofluids, *Phys. Rev. E* **62**, 2985 (2000).
- [31] T. John, K. May, and R. Stannarius, Meniscus of a ferrofluid around a vertical cylindrical wire carrying electric current, *Phys. Rev. E* **83**, 056308 (2011).
- [32] E. O. Dias and J. A. Miranda, Azimuthal field instability in a confined ferrofluid, *Phys. Rev. E* **91**, 023020 (2015).
- [33] C.-Y. Chen and T.-S. Lin, in *Advances in Computational Fluid-Structure Interaction and Flow Simulation*, edited by Y. Bazilevs and K. Takizawa (Springer Nature, Basel, 2016).
- [34] C.-Y. Chen, W.-L. Wu, and J. A. Miranda, Magnetically induced spreading and pattern selection in thin ferrofluid drops, *Phys. Rev. E* **82**, 056321 (2010).
- [35] R. M. Oliveira, J. A. Miranda, and E. S. G. Leandro, Ferrofluid patterns in a radial magnetic field: Linear stability, nonlinear dynamics, and exact solutions, *Phys. Rev. E* **77**, 016304 (2008).
- [36] R. M. Oliveira and J. A. Miranda, Fully nonlinear simulations of ferrofluid patterns in a radial magnetic field, *Phys. Rev. Fluids* **5**, 124003 (2020).
- [37] Z. Yu and I. C. Christov, Tuning a magnetic field to generate spinning ferrofluid droplets with controllable speed via nonlinear periodic interfacial waves, *Phys. Rev. E* **103**, 013103 (2021).
- [38] R. M. Oliveira, I. M. Coutinho, P. H. A. Anjos, and J. A. Miranda, Shape instabilities in confined ferrofluids under crossed magnetic fields, *Phys. Rev. E* **104**, 065113 (2021).
- [39] P. O. S. Livera, P. H. A. Anjos, and J. A. Miranda, Magnetically induced interfacial instabilities in a ferrofluid annulus, *Phys. Rev. E* **104**, 065103 (2021).
- [40] S. H. Strogatz, *Nonlinear Dynamics and Chaos: With Applications to Physics, Biology, Chemistry, and Engineering* (Addison-Wesley, New York, 1994).
- [41] M. C. Cross and P. C. Hohenberg, Pattern formation outside of equilibrium, *Rev. Mod. Phys.* **65**, 851 (1993).
- [42] P. Manneville, *Dissipative Structures* (Springer-Verlag, Berlin, 1990).
- [43] T. H. Beeson-Jones and A. W. Woods, On the selection of viscosity to suppress the Saffman-Taylor instability in a radially spreading annulus, *J. Fluid Mech.* **782**, 127 (2015).
- [44] P. H. A. Anjos and S. Li, Weakly nonlinear analysis of the Saffman-Taylor problem in a radially spreading fluid annulus, *Phys. Rev. Fluids* **5**, 054002 (2020).
- [45] C. Flament, S. Lacis, J.-C. Bacri, A. Cebers, S. Neveu, and R. Perzynski, Measurements of ferrofluid surface tension in confined geometry, *Phys. Rev. E* **53**, 4801 (1996).
- [46] C. Flament, G. Pacitto, J.-C. Bacri, I. Drikis, and A. Cebers, Viscous fingering in a magnetic fluid. I. Radial Hele-Shaw flow, *Phys. Fluids* **10**, 2464 (1998).
- [47] G. Pacitto, C. Flament, J.-C. Bacri, and M. Widom, Rayleigh-Taylor instability with magnetic fluids: Experiment and theory, *Phys. Rev. E* **62**, 7941 (2000).
- [48] N. J. Hillier and D. P. Jackson, Width of a ferrofluid finger: Hysteresis and a double energy minimum, *Phys. Rev. E* **75**, 036314 (2007).
- [49] R. M. Oliveira and J. A. Miranda, Stretching of a confined ferrofluid: Influence of viscous stresses and magnetic field, *Phys. Rev. E* **73**, 036309 (2006).

- [50] S. A. Lira and J. A. Miranda, Nonlinear traveling waves in confined ferrofluids, *Phys. Rev. E* **86**, 056301 (2012).
- [51] Z. Yu and I. C. Christov, Long-wave equation for a confined ferrofluid interface: Periodic interfacial waves as dissipative solitons, *Proc. R. Soc. A* **477**, 20210550 (2021).
- [52] J. M. Ginder, Behavior of magnetorheological fluids, *MRS Bull.* **23**, 26 (1998).
- [53] G. Bossis, S. Laciş, A. Meunier, and O. Volkova, Magnetorheological fluids, *J. Magn. Magn. Mater.* **252**, 224 (2002).